

CrossMark
click for updatesCite this: *J. Mater. Chem. A*, 2016, 4, 2670

Hydrogen treated anatase TiO₂: a new experimental approach and further insights from theory†

Manan Mehta,^{af} Nisha Kodan,^b Sandeep Kumar,^c Akshey Kaushal,^b Leonhard Mayrhofer,^{de} Michael Walter,^{de} Michael Moseler,^{de} Avishek Dey,^f Satheesh Krishnamurthy,^f Suddhasatwa Basu^{*a} and Aadesh P. Singh^{*b}

Hydrogenated TiO₂ (H:TiO₂) is intensively investigated due to its improvement in solar absorption, but there are major issues related to its structural, optical and electronic properties and therefore an easily compatible method of preparation is much needed. In order to clarify this issue we studied TiO₂ nanocrystals under the partial pressure of hydrogen to modify the structural, optical and electrical properties and to significantly improve the photocatalytic and photoelectrochemical performance. The hydrogen treated TiO₂ nanocrystals contained paramagnetic Ti³⁺ centers and exhibited a higher visible light absorption cross-section as was confirmed by electron paramagnetic resonance diffuse reflectance spectra measurements and X-ray photoelectron spectroscopy. The hydrogen annealed samples showed a noticeable improvement in photocatalytic activity under visible light ($\lambda > 380$ nm) which was demonstrated by the degradation of methylene blue dye and an improved photoelectrochemical response in terms of high photocurrent density. *Ab initio* simulations of TiO₂ were performed in order to elucidate the conditions under which localized Ti³⁺ centres rather than delocalized shallow donor states are created upon the reduction of TiO₂. Randomly distributed oxygen vacancies lead to localized deep donor states while the occupation of the oxygen vacancies by atomic hydrogen favours the delocalized shallow donor solution. Furthermore, it was found that localization is stabilized at high defect concentrations and destabilized under external pressures. In those cases where localized Ti³⁺ states are present, the DFT simulations showed a considerable enhancement of the visible light absorption as well as a pronounced broadening of the localized Ti³⁺ energy levels with increasing defect concentration.

Received 8th September 2015
Accepted 15th January 2016

DOI: 10.1039/c5ta07133j

www.rsc.org/MaterialsA

1. Introduction

Nanosized titanium dioxide (TiO₂) in the anatase phase has been extensively used in solar driven photocatalytic processes for hydrogen production and water decontamination.^{1–3} However, its large bandgap (~3.2 eV) requires light below 388 nm to create an electron–hole pair and limits the overall

efficiency. Therefore, in order to increase absorption of TiO₂ for natural solar radiation, a variety of techniques have been reported such as metal ion doping,^{4,5} anion doping,^{6,7} noble metal loading,^{8,9} addition of electron donors,¹⁰ metal ion-implantation¹¹ and self-doping that produce Ti³⁺ species¹² *etc.* At present, anion-doped TiO₂ (especially nitrogen doping in TiO₂) exhibits the greatest optical response to the visible region, due to its modified electronic transition from the dopant 2p orbitals to the Ti3d orbitals which is responsible for the visible light absorption. However, N-doped TiO₂ still has no sufficient absorption in the visible region.⁶

Over the past few years hydrogen induced modification in metal oxide semiconductors has been of substantial interest due to their higher photocatalytic performance. Hydrogen treatment techniques play a key role in tailoring the optical and electronic properties of metal oxide thin films and nanoparticles. Various hydrogen treatment processes such as high pressure hydrogen annealing,^{13,14} electrochemical hydrogenation^{15,16} and hydrogen plasma^{17,18} for making black metal oxide nanoparticles and thin films have been used to modify the optical, electrical and photocatalytic properties. Different

^aDepartment of Chemical Engineering, Indian Institute of Technology, HauzKhas, New Delhi-110016, India. E-mail: sbasu@iitd.ac.in; Fax: +91 11 26581120; Tel: +91 11 26591035

^bDepartment of Physics, Indian Institute of Technology, Hauz Khas, New Delhi-110016, India. E-mail: aadshp1982@gmail.com

^cDepartment of Chemistry, Indian Institute of Technology, Hauz Khas, New Delhi-110016, India

^dFraunhofer IWM, Wöhlerstr. 11, D-79108 Freiburg, Germany

^eUniversity of Freiburg, FMF - Freiburg Materials Research Center, Stefan-Meier-Str. 21, D-79104 Freiburg, Germany

^fDepartment of Engineering and Innovation, The Open University, Milton Keynes, MK7 6AA, UK

† Electronic supplementary information (ESI) available. See DOI: 10.1039/c5ta07133j



hydrogen treatment processes lead to different properties of the hydrogen modified TiO₂ materials. Chen *et al.* reported that TiO₂ nanocrystals treated in a hydrogen atmosphere under a 20 bar H₂ atmosphere for 5 days showed a colour change to black with a reduction in the bandgap energy up to ~1.54 eV.^{13,14} They have reported that the change in colour is due to the surface disorder of TiO₂ nanoparticles. The colour change in the metal oxide due to hydrogen depends upon the hydrogen treatment temperature, the partial pressure and also on the nature of hydrogen species, while in the work of Chen *et al.*¹³ the narrowing of the band gap could be traced back to the surface disorder without the formation of Ti³⁺ centres; other studies¹² found strong evidence that lattice defects such as oxygen vacancies can form localized Ti³⁺ centres within the TiO₂ bandgap. Moreover, in the work of Wang *et al.*¹⁷ hydrogen doping created a high density of delocalized Ti3d electrons leading to improved charge transport properties.

Different hydrogen treatment processes lead to different properties of the hydrogen modified TiO₂ materials. Hydrogen annealing of TiO₂ under high pressure did not show any detectable Ti³⁺ states, but, produces disordered surface layers over the crystalline TiO₂ particles forming a core-shell structure.¹³ Reduction of TiO₂ particles in a H₂ atmosphere at 500 °C shows the formation of a crystalline core/amorphous shell (TiO₂@TiO_{2-x}H_x) structure with about 83% absorption of solar light.¹⁷ Hydrogen plasma treatment in TiO₂ nanotubes has been observed to result in simultaneously incorporated Ti³⁺ and -OH groups.¹⁹ Hydrogen plasma treated ALD grown TiO₂ thin films also show the formation of Ti³⁺ states.²⁰ Electrochemical H⁺ doping in TiO₂ films also exhibits the presence of Ti³⁺ and -OH that may lead to additional electronic states in the band gap and shift light absorption to the visible region.¹⁸ Different hydroxyl groups present on TiO₂ surfaces are supposed to participate in electron trapping in TiO₂ and other oxides.²¹ Reduction of TiO₂ and -OH group formation has also been reported in theoretical hybrid density functional (B3LYP) based studies on hydrogen doping in TiO₂.^{19,22}

Although, encouraging results on hydrogen treated TiO₂ have been obtained,^{13,14} a detailed understanding of the role of hydrogen species (*e.g.* atomic, molecular or ionic hydrogen) and an easily scalable process to tailor the required hydrogen and to modify the structural, electronic energy band structure of TiO₂ to realize the improvements in photocatalytic properties is of utmost importance.

Therefore, in this work we used 5% H₂ in Ar to modify optical absorption by creating defect/disordered states in the TiO₂ lattice and studied photocatalytic degradation of methylene blue to be used in photoelectrochemical water splitting applications. This is the new experimental approach to tailor the optical, electrical and photocatalytic properties of TiO₂ in a controlled way. The hydrogen treated brownish TiO₂ nanoparticles with long-wavelength absorption showed much better performance in photocatalytic decomposition of methylene blue and phenol than pure TiO₂ nanocrystals. In our hydrogen treated TiO₂ samples, localized Ti³⁺ centres were identified, which explain the origin of the modified electronic structure. In order to further elucidate the conditions under which localized Ti³⁺ states rather than delocalized shallow donor states are

formed upon hydrogen treatment, *ab initio* calculations within the density functional theory (DFT) of TiO₂ with varying concentrations of oxygen vacancies and oxygen vacancies occupied by atomic hydrogen were performed.

2. Experimental procedures

2.1 Synthesis of TiO₂ nanoparticles

Pristine TiO₂ nanocrystals were prepared by a wet chemical method using titanium tetra-isopropoxide, ethanol, hydrochloric acid and deionized water as reported earlier.²³ In brief, 25 mL deionized water mixed with 1 mL hydrochloric acid was added slowly to 10 mL of titanium tetra-isopropoxide with continuous stirring in an ice bath. A white precipitate solution was obtained, which was filtered and heated in air at 80 °C to evaporate extra water. After evaporation of water, the white precipitate was sintered at 400 °C for 4 h. For the hydrogen treatment under partial pressure, the annealing chamber was pumped down to 2.0 × 10⁻⁶ Torr and 20 sccm. 5% H₂ balanced Ar was introduced into the chamber while maintaining the chamber pressure at 2 × 10⁻² Torr. The annealing temperature was set at 300 °C for 10, 20 and 30 h followed by cooling down for 1 h.

2.2 Materials characterization

Glancing angle X-ray diffraction and Raman analysis were carried out on a Philip's X'Pert PRO-PW vertical system operating in reflection mode using Cu K α ($\lambda = 0.15406$ nm) radiation and an Invia Raman microscope using a 514 nm argon ion laser pulse for excitation, respectively. To understand the optical behavior, the UV-visible spectra were measured on a Perkin-Elmer Lambda 35 UV visible spectrometer in the wavelength range of 200–800 nm. About 50 mg of TiO₂ nanocrystals were pressed into a small sample container to make a flat surface and uniform density in a 'Praying Mantis' diffuse reflection accessory. Fourier transform infrared spectroscopy (FTIR) analysis was performed at room temperature using a Nicolet 5700 spectrometer in transmission mode in the wavenumber range of 500–4000 cm⁻¹. The spectroscopic grade KBr pellets were used for collecting the spectra with a resolution of 4 cm⁻¹ performing 32 scans. All the measurements were conducted under ambient conditions in air. TEM (FEI-Technai-G20 with a LaB6 filament, operating at 200 keV) was used to study the size and structural properties of nanoparticles. Proton Nuclear magnetic resonance (¹H-NMR) measurements were carried out to investigate the effect of hydrogen treatment on H:TiO₂ using a Nuclear Magnetic Resonance Spectrometer (JEOL-JNM-ECA Series (Delta V4.3)-400 MHz-FT-NMR). The EPR spectra were recorded on a Bruker EPR 100d X-band spectrometer for pristine and H:TiO₂ samples through the EPR cavity. *G* values were calibrated using a di(phenyl)-(2,4,6-trinitrophenyl)iminoazanium (DPPH) sample. The parameters utilized in EPR measurements are as follows: center field, 3512 G; frequency, 9.74 GHz; microwave power, 20 mW. X-ray photoelectron spectroscopy (XPS, Kratos, XSAM 800) was carried out with non-monochromatic Mg ($h\nu = 1253.6$ eV) radiation. All binding energies were calibrated by referencing to the C1s peak at 284.6 eV. The deconvolution of the Ti peaks was performed through CASA XPS software.



2.3 Photocatalytic experiments

The photocatalytic performance of pristine and hydrogen treated TiO₂ samples was evaluated by observing their abilities to degrade the methylene blue (MB) dye, which is adopted as a representative organic pollutant in wastewater, in aqueous solution under simulated visible irradiation induced by using a 100 W tungsten lamp equipped with a UV cut-off filter to remove the radiation below 380 nm.

In a typical visible-light photocatalytic experiment, the catalyst (30 mg) was dispersed in a 100 mL aqueous solution of MB (10 μM) and the obtained catalyst suspensions were magnetically stirred at 250 rpm in the dark for 40 min to ensure adsorption/desorption equilibrium between the catalyst and organic dye. The catalyst suspension was subsequently irradiated with a 100 W tungsten lamp. A sufficient dye solution (2 mL) of the suspension was extracted and centrifuged after every 10 min during the course of 100 min irradiation to remove the residual catalyst particulates for analysis. Control experiments were performed either without the catalyst or in the dark to attest that the degradation reaction is solely by a photocatalytic process. The photodegradation efficiency was monitored by measuring the change in intensity of the characteristic absorbance peak of MB at 664 nm using a Shimadzu UV-2450 spectrometer with 10 mm path length quartz cells. The photodegradation efficiency (D) of each catalyst was determined using the following equation:

$$D(\%) = 100 \times (C_0 - C)/C_0 \quad (1)$$

here C is the concentration of MB at the time interval t and C_0 is the concentration after the adsorption equilibrium is reached before irradiation.

2.4 Photoelectrochemical and electrochemical impedance spectroscopy

For photoelectrochemical and electrochemical impedance spectroscopy (EIS) measurements, thin films from TiO₂ powders were prepared using sol-gel spin coating techniques. These measurements were carried out in a three-electrode photoelectrochemical cell using pristine and H:TiO₂ thin films as the working electrode, Pt as the counter electrode and Ag/AgCl as the reference electrode in a 1 M NaOH electrolyte (pH = 13.6). The photoelectrochemical cell was controlled using a CIMPS-2 (Controlled Intensity Modulated Photospectroscopy) system consisting of a Zennium Electrochemical Workstation (X-Pot Potentiostat). For photoelectrochemical measurements, linear sweep voltammetry scans under dark and illumination were carried out in the potential range of -1.0 to $+1.0$ V *versus* Ag/AgCl with a scan rate of 20 mV s^{-1} . The illumination source was a white light source ($\lambda > 380 \text{ nm}$) having an output illumination intensity of 100 mW cm^{-2} . The electrochemical impedance spectroscopy (EIS) measurements were carried out in the frequency range from 100 kHz to 0.01 Hz with an AC signal amplitude of 10 mV under open bias conditions (*i.e.* 0.0 V *versus* Ag/AgCl reference electrode) to obtain the physical parameters such as flat band potential, carrier concentration, carrier conductivity, charge separation, and recombination processes.

2.5 *Ab initio* simulations

For the *ab initio* calculations we used the Vienna *ab initio* simulations package (VASP).²⁴ In VASP the valence electrons are described by using a plane wave basis set and the core electrons are taken into account using the projector-augmented wave formalism.^{25,26} All simulations were carried out within the PBE + U framework.²⁷ Here, the properties of the strongly correlated d-electrons are corrected by using a Hubbard-like term for the onsite Coulomb interactions. We used a value of 4 eV for the Hubbard parameter U very close to the choice used in previous studies on n-type defects in TiO₂.^{28–31} For the energy cut-off that defines the plane wave basis set we used a value of 500 eV. For modelling hydrogen treated anatase TiO₂ with different levels of disorder, we used $3 \times 3 \times 1$ super cells. Reciprocal space was sampled by using a $3 \times 3 \times 4$ grid including the Γ point and by using a Gaussian smearing with a width of 0.1 eV. Structural relaxations were performed until all forces were smaller than 0.02 eV \AA^{-1} . The unit cell vectors were optimized simultaneously with the ion positions until pressures smaller than 1.0 kbar (0.1 GPa) were reached. In those cases where external pressure was applied the unit cell vectors were varied until the target pressures were reached within the same accuracy of at least 1.0 kbar.

In order to calculate optical absorption coefficients we determined the frequency dependent dielectric function of the material by *ab initio* methods. The wavelength dependent absorption coefficient $\alpha(\lambda)$ is given by³²

$$\alpha(\lambda) = \frac{2\pi}{\lambda} \sqrt{2(|\epsilon| - \epsilon_r)} \quad (2)$$

where ϵ is the complex frequency dependent dielectric function and ϵ_r is its real part.

The imaginary part ϵ_i of the dielectric function was calculated by a summation over matrix element products between the occupied and unoccupied Kohn–Sham eigenstates using the VASP software package as described by Gajdoš *et al.*³³ The real part of the dielectric function was derived *via* the Kramers–Kronig relation. Off-diagonal elements of the dielectric function were found to be strongly suppressed and were hence ignored. An average over the diagonal elements of ϵ was used as an input for the calculation of the absorption coefficient in order to take into account the absence of any predominant orientation in polycrystalline materials.

3. Results and discussion

To determine the crystal structure and possible phase changes after hydrogen treatment, X-ray diffraction (XRD) spectra were collected from the pristine and hydrogen treated TiO₂ nano-crystal samples at 300 °C for different times (Fig. 1(a)). All the peaks in the XRD pattern of pristine and H:TiO₂ exhibited feature characteristics of the tetragonal anatase TiO₂ crystallographic phase. Major peaks are observed at 2θ angles of 25.3, 37.84, 48.07, 53.95, and 55.10° with d_{hkl} of 3.51, 2.37, 1.89, 1.69, and 1.66 Å corresponding to diffraction from planes (101), (044), (200), (105) and (211), respectively. Therefore, the tetragonal anatase phase of TiO₂ has been retained without any



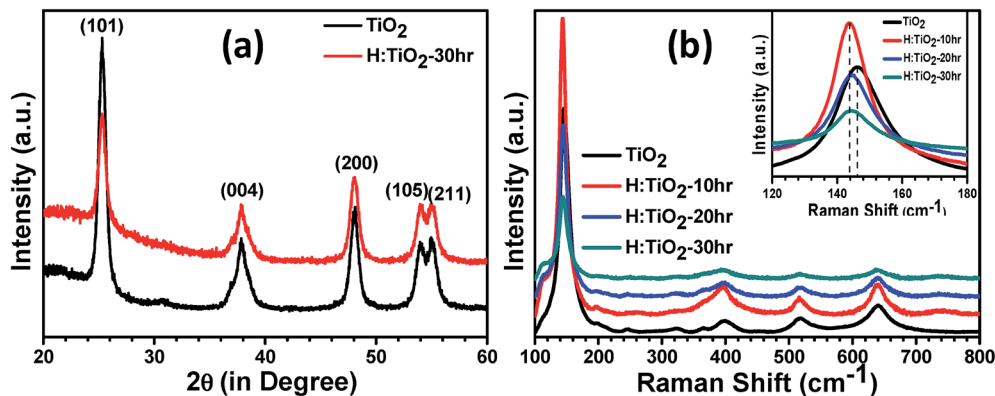


Fig. 1 (a) XRD and (b) Raman spectra of the pristine and hydrogen treated TiO₂ nanocrystals.

structural transformation even after hydrogen treatment at 300 °C for 30 hours. The annealing of TiO₂ in hydrogen ambient may affect TiO₂ in two ways. It can lead to the formation of TiH₂ (ref. 34) or the hydrogen would react with the oxygen in TiO₂ leading to the formation of lattice defects.³⁵ Since XRD data did not indicate any peak corresponding to TiH₂, the reduction of TiO₂ resulting in the formation of lattice defects such as oxygen vacancies is more likely. Both TiO₂ and H:TiO₂ samples show similar diffraction patterns (Fig. 1(a)). The slightly weaker XRD diffraction peak intensity in H:TiO₂ indicates that the crystallinity of H:TiO₂ upon hydrogen treatment is decreased due to defect generation and/or some degree of surface disorder.

To further study any change in the phase structure after hydrogen treatment, Raman spectroscopy was performed on pristine and H:TiO₂ as shown in Fig. 1(b). Well-resolved TiO₂ Raman peaks were observed at 144 cm⁻¹ (B_{1g}), 398 cm⁻¹ (B_{1g}), 515 cm⁻¹ (E_g), and 640 cm⁻¹ (E_g) in the spectra of all samples, indicating that anatase nanoparticles are the predominant species. Only the peak expected at 147 cm⁻¹ (E_g) was not visible, which may be suppressed by a much stronger TiO₂ peak at 144 cm⁻¹ (B_{1g}) line.³⁶ No major effects of hydrogen treatment with time were observed on the position of peaks in Raman spectra, *i.e.*, the anatase structure is retained after hydrogen treatment. However, peak broadening in the H:TiO₂ samples was observed in all the peaks in comparison to pristine. Such peak broadening in the Raman spectrum is assigned to structural changes in H:TiO₂ indicating the formation of oxygen vacancies and other defects in the lattice.

Fig. 2 shows the diffuse reflectance spectra (DRS) of pristine and hydrogen treated black TiO₂ nanocrystals. A steep increase in absorption at wavelengths shorter than 375 nm can be attributed to the intrinsic band gap of crystalline anatase TiO₂. H:TiO₂ samples with different durations of treatment show a significant shift of absorption edge towards higher wavelength sliding to visible light absorption. Especially for the H:TiO₂ sample treated in hydrogen for 30 h, the increase in absorption is observed in the wavelength range of 375–675 nm. The increased absorption is much higher as compared to other modification techniques used for TiO₂ layers. The calculated values of the band gap energy from diffusivity reflectance (inset (a) of Fig. 2) show that the band gap of the pristine TiO₂

nanocrystals is approximately 3.30 eV, slightly higher than that of bulk anatase TiO₂. The onset of light absorption for the hydrogen treated brownish TiO₂ nanocrystals was lowered to about 2.59 eV. A digital photograph of pristine and hydrogen treated TiO₂ nanocrystals is shown in the inset of Fig. 2(b) and (c), clearly showing the drastic change in the optical properties upon hydrogen treatment.

In order to investigate the changes in the microstructure upon hydrogen treatment, high-resolution transmission electron microscopy (HR-TEM) studies were carried out on the pristine and hydrogen treated brown TiO₂ nanocrystals as shown in Fig. 3. The pristine TiO₂ nanocrystal is completely crystalline, displaying clearly resolved and well-defined lattice fringes, terminating quite sharply at the surface of the nanocrystals (Fig. 3(a)). However, HR-TEM images of hydrogen treated black H:TiO₂ nanoparticles exhibit a disordered amorphous shell layer structure around the crystalline TiO₂ core resulting in crystalline core/amorphous shell (TiO₂@H:TiO₂) nanostructures as shown in Fig. 3(b). The average size of individual nanoparticles is approximately 15 nm in diameter. The disordered layer on the surface of H:TiO₂ is ≈ 1–2 nm in

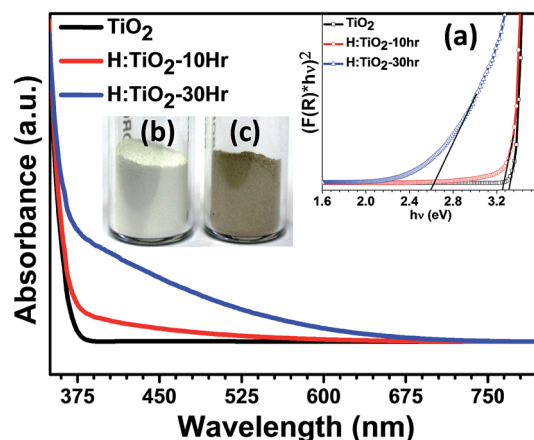


Fig. 2 Diffuse reflection spectra of pristine and hydrogen treated TiO₂ nanocrystals. The inset (a) shows the transformed Kubelka–Munk spectrum. (b) and (c) show the actual digital photograph of pristine and hydrogenated TiO₂ nanocrystals.



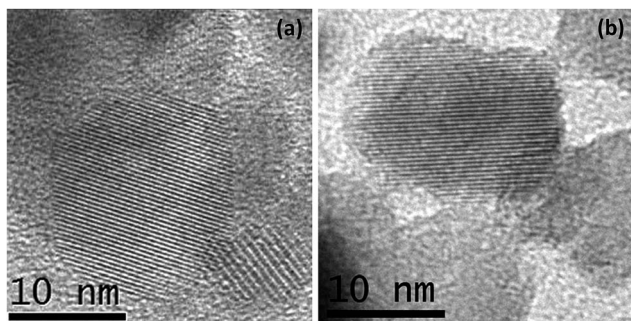


Fig. 3 HR-TEM images of (a) pristine and (b) hydrogen treated TiO_2 nanocrystals for 30 h.

thickness coated on a crystalline core after the hydrogen treatment for 30 h. From these values we can estimate that the fraction of the disordered material is between 15 and 25% of the total volume.

More insights into chemical changes caused by the hydrogen treatment on TiO_2 were obtained by Fourier transform infrared (FT-IR) spectroscopic measurements. The results are shown in Fig. 4(a). FT-IR spectra of both pristine and hydrogen treated samples show similar absorption features from 500 cm^{-1} to 4000 cm^{-1} and exhibit OH absorption bands near the 1635 cm^{-1} and 3400 cm^{-1} region. The characteristic feature of the spectrum symmetric stretching vibrations of the Ti–O bonds is the presence of a band in the region of $400\text{--}800\text{ cm}^{-1}$ which is due to the TiO_6 octahedra. After hydrogen treatment, the intensity of OH absorption bands is decreased near the 3400 cm^{-1} which suggests that the hydrogen treatment prevents the passivation of more O dangling bonds as this would otherwise increase the absorption. The wider OH absorption band in H: TiO_2 indicates that the H: TiO_2 surface provides the more diverse environment for the absorption of OH bands than the pristine TiO_2 .¹⁴

We further examined TiO_2 and H: TiO_2 by ^1H NMR measurements to study the role of hydrogen treatment under partial pressure conditions. Fig. 4(b) shows the ^1H NMR data of pristine and H: TiO_2 nanocrystals with broad peaks at chemical shifts of 3.74 and 3.87 ppm, respectively. The ^1H NMR spectra of

H: TiO_2 samples show a large line width which may be due to the incorporation of H at bridging sites at the disordered surface produced during the hydrogen treatment under partial pressure, or may be due to the bridging sites located on different crystallographic planes on the surface.^{37,38} Additionally, pristine TiO_2 shows two narrow peaks at chemical shifts of +0.22 ppm and -0.77 ppm . However, the hydrogen treated H: TiO_2 sample shows a pronounced additional peak at a chemical shift of -1.07 ppm . This new peak at $\delta = -1.07\text{ ppm}$ in H: TiO_2 is probably due to the presence of weakly bound hydrogen atoms as a result of the hydrogen treatment process and may provide an explanation for the enhanced hydrogen mobility in black TiO_2 .³⁷ Considering the theoretical studies, we may conclude that the weakly bound hydrogen atoms are frequently absorbed by oxygen vacancies in H: TiO_2 .^{39–41}

Electron paramagnetic resonance (EPR) spectroscopy was used to determine the presence of unpaired electron spins corresponding to localized Ti^{3+} centers. To provide a clear picture of the existence of Ti^{3+} in hydrogen treated H: TiO_2 , we performed the EPR measurement on TiO_2 treated in 5% H_2 mixed Ar at $300\text{ }^\circ\text{C}$ for 30 hours. As shown in Fig. 5, the pristine TiO_2 possesses a very weak resonance signal at a g -value of 2.08 which results from surface adsorbed O_2^- from air.^{42,43} This confirms that pristine TiO_2 contains almost only Ti^{4+} ($3d^0$) ions and exhibits weak unpaired electron signals. For the sample treated with hydrogen for 30 h, a strong EPR signal was observed with a g value of 1.95, which is a characteristic of paramagnetic Ti^{3+} centers.¹⁷ The formation of Ti^{3+} centers is frequently explained by the generation of oxygen vacancies during the reduction of TiO_2 by hydrogen treatment. The strong EPR signal in H: TiO_2 confirms that the vacuum hydrogen treated TiO_2 nanocrystal sample contains a large concentration of Ti^{3+} and oxygen vacancies.

XPS measurements were carried out on both pristine and hydrogen treated TiO_2 nanoparticles to understand the surface chemical bonds. In order to understand the chemical composition, peak position and hence the electronic properties, the $\text{Ti}2p_{3/2}$ core level spectra were fitted with a mixture of Gaussian and Lorentzian line shapes, where Gaussian takes care of instrumental broadening and Lorentzian for the core hole life time with a Shirley background. Fig. 6(a) and (b) show a peak at

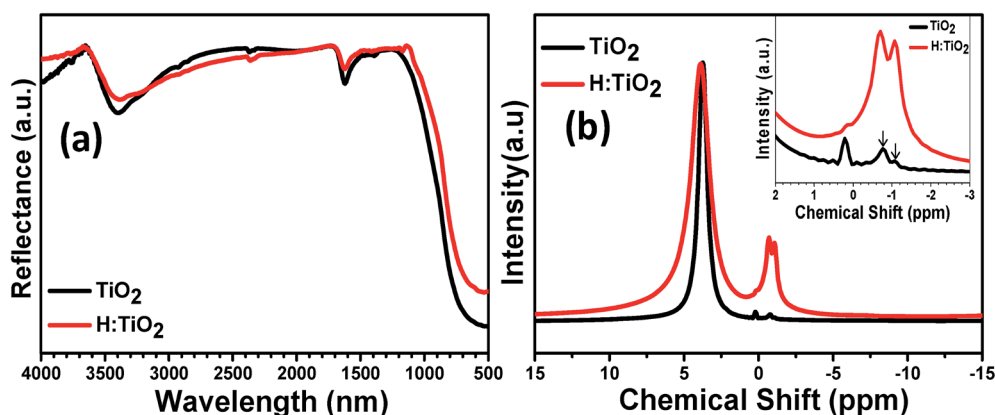


Fig. 4 (a) FTIR and (b) ^1H NMR spectra of the pristine and hydrogen treated TiO_2 nanocrystals.



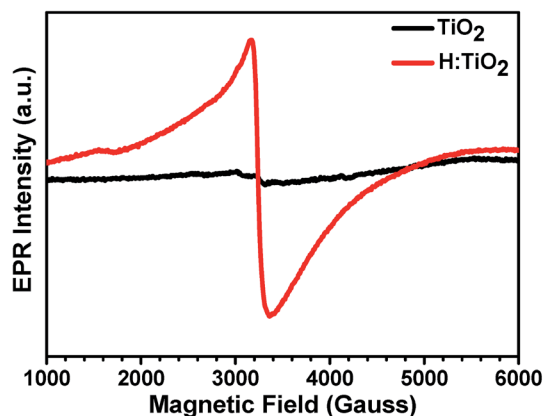


Fig. 5 EPR spectra of pristine and hydrogen treated TiO_2 samples recorded at 300 K. The g values of the H: TiO_2 sample indicated in the figures correspond to the minima or maxima of the different Ti^{3+} EPR lines.

a binding energy of 459 ± 0.1 eV which is attributed to Ti^{4+} states for both TiO_2 and hydrogen treated TiO_2 .^{44,45} However, for hydrogen treated TiO_2 a new peak is observed at a binding

energy of 456.2 ± 0.1 eV which is attributed to Ti^{3+} as shown in Fig. 6(b), indicating a different bonding environment which is due to hydrogen treatment that creates disorder in the lattice, resulting in the near surface Ti^{3+} . Fig. 6(c) and (d) represent the O1s spectra of TiO_2 systems. The peak at a binding energy of 530.4 ± 0.1 eV corresponds to O–Ti bonds in titanium dioxide. The second component is broader at a binding energy of 531.6 ± 0.1 eV due to Ti–OH bonds.⁴⁶ The reduction in the hydroxyl component could be due to the combination of desorption of hydroxyl groups and the influence of hydrogen treatment.

It has been further proposed by experimental¹⁷ and theoretical^{39–41} studies that atomic hydrogen gets preferably absorbed at the oxygen vacancies in TiO_2 . In the work of Wang *et al.*,¹⁷ it was concluded that all oxygen vacancies get occupied by atomic hydrogen leading to the conversion of stoichiometric TiO_2 to the composition $\text{TiO}_{2-x}\text{H}_x$. This finding was rationalized by the absence of any localized Ti^{3+} centers which are typically formed near oxygen vacancies. This reasoning is supported by our simulations as will be discussed later on. Since we do find a strong EPR signal of localized Ti^{3+} states in our samples and as the samples were synthesized under rather mild hydrogen conditions, it can be concluded that the majority of

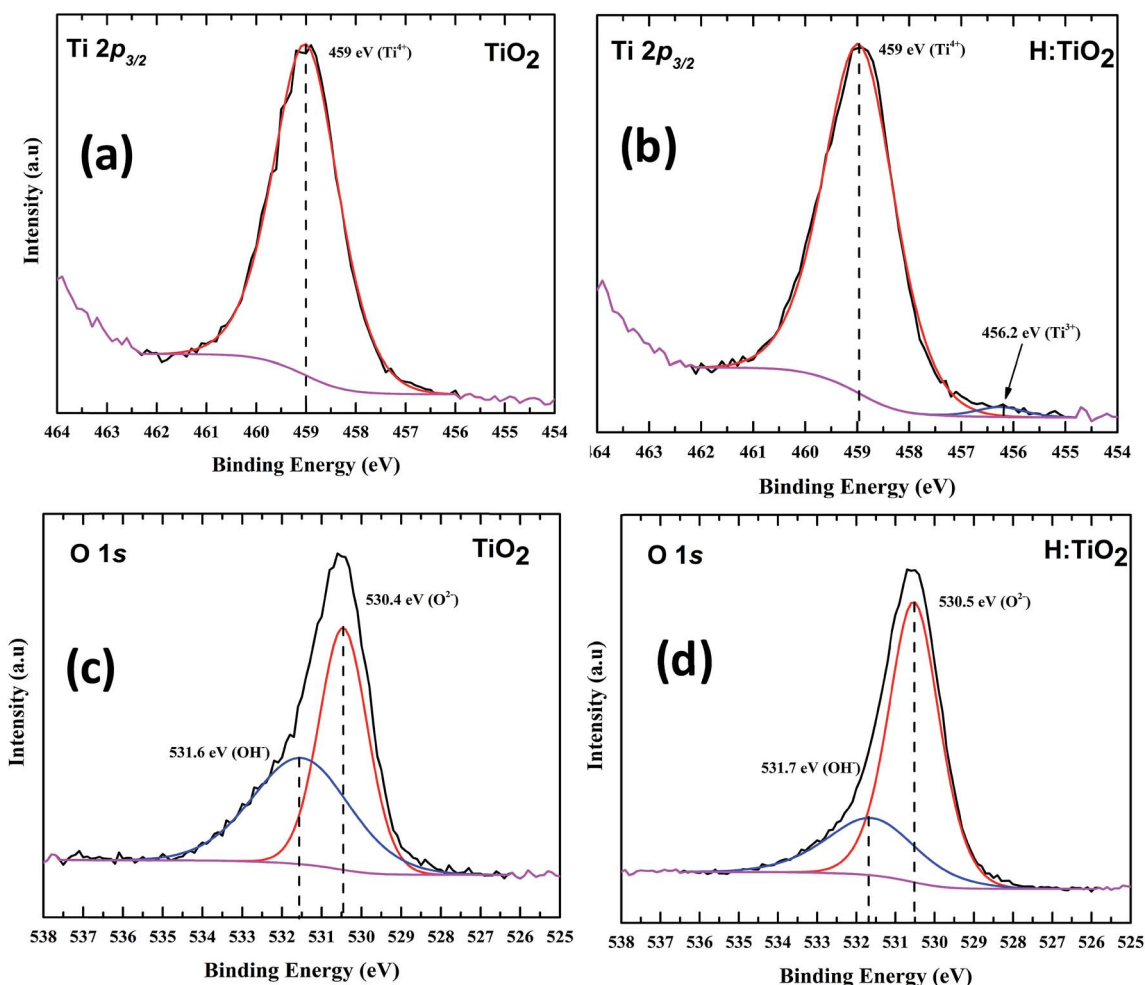


Fig. 6 XPS spectra of (a) $\text{Ti}2p$ of pristine TiO_2 , (b) hydrogen treated TiO_2 shows the presence of Ti^{3+} (c) O1s of TiO_2 and (d) O1s of hydrogen treated TiO_2 .



oxygen vacancies are not occupied by atomic hydrogen, at least in our case. As previous experimental studies^{14,41,47} and our simulation results discussed below show, a high concentration of oxygen vacancies and Ti^{3+} centers introduces occupied mid-gap states, which substantially narrow the electronic band gap of TiO_2 . Photoexcitation of these states correspondingly leads to a narrow optical band gap in agreement with our DRS measurements (Fig. 2) and potentially to enhanced visible-light photocatalytic activity.

The experimental results clearly indicate the relevance of enhanced visible light absorption which is one of the main reasons for improving the photoelectrochemical performance of TiO_2 . It is important to understand the crucial role of hydrogen treatment in forming localized electronic mid-gap states in the form of Ti^{3+} centers as experimentally observed in this work. In different studies oxygen vacancies (pristine V_O or occupied by atomic hydrogen H_O) have been investigated as prototypical defects associated with the reduction of TiO_2 by hydrogen in order to elucidate the modification of the electronic structure and optical absorption properties. In many cases,^{47,48} the blackening of hydrogen treated TiO_2 is traced back to the formation of localized Ti^{3+} states in the TiO_2 band gap enabling the absorption of photons from the visible light spectrum. However, hydrogen treatment of TiO_2 can also lead to the generation of a high density of occupied delocalized electronic states which act as shallow electron donors and hence lead to a high concentration of mobile charge carriers.¹⁷

In order to elucidate the conditions which favor the generation of localized or delocalized electrons after the reduction of TiO_2 we studied in this work the energetics of localized and delocalized states induced by different defect types, in terms of defect concentration and external pressure. We have used anatase supercells of the composition $\text{Ti}_{36}\text{O}_{72}$ which are generated by a $3 \times 3 \times 1$ repetition of the tetragonal anatase

unit cell. The dimensions of the optimized defect free supercell are $1.17 \times 1.17 \times 0.97 \text{ nm}^3$. Different supercell compositions for oxygen vacancies $\text{Ti}_{36}\text{O}_{72-x}$ (V_O defects), and hydrogen saturated oxygen vacancies $\text{Ti}_{36}\text{O}_{72-x}\text{H}_x$ (H_O defects), $x = 0, 1, 6, 10$, were considered. These correspond to defect concentrations of 0, 1.4, 8.3 and 13.9% with respect to the number of oxygen atoms. The corresponding structures for the case of V_O defects are shown in Fig. 7. The disorder in the material was modeled by placing the lattice defects on random sites in the super cell. The positions of the impurities were chosen such that defects on adjacent sites are avoided since these configurations are energetically disfavored.

We start the discussion of the *ab initio* calculations with the results concerning the conditions that favor or disfavor the generation of localized Ti^{3+} centers or delocalized shallow donor states due to V_O and H_O defects. As a measure for the stability of the localized Ti^{3+} states we calculated the localization energy $E_{\text{loc}} = \frac{E_{\text{deloc}} - E_{\text{loc}}}{\#(\text{defects})}$ for varying concentrations of V_O and H_O defects and varying external pressure. Here E_{deloc} and E_{loc} are the ground state energies of the defective TiO_2 unit cells with delocalized and localized Ti^{3+} states, respectively, and $\#(\text{defects})$ is the number of defects per unit cell. Hence, positive values of E_{loc} indicate that localization is more favorable than delocalization. We find that the localized states tend to be more stable at higher defect concentrations for both defect types (Fig. 8(a)). At higher concentrations of H_O and V_O defects similar localization energies in the range from about 0.2 to 0.45 eV are obtained in both cases, indicating the formation of localized Ti^{3+} centers. However, at the lowest considered defect concentration, corresponding to a single defect in the $3 \times 3 \times 1$ supercell, the behavior of the two defect types deviates substantially. Here, the delocalized solution is slightly favored in the case of the H_O defect by 0.03 eV, while the V_O defect leads to a localized solution with $E_{\text{loc}} = 0.22 \text{ eV}$. The latter value is in reasonable agreement with hybrid functional calculations²² where $E_{\text{loc}} = 0.17 \text{ eV}$ was found. The formation of a delocalized solution in the case of a low concentration of H_O defects is in good agreement with the experimental work of Wang *et al.*¹⁷ who assumed that the substitution of oxygen by hydrogen leads to the observed high densities of delocalized mobile charge carriers. Selected HSE06 hybrid functional calculations confirmed the delocalized ground state of the electron donated by the H_O defect at the lowest considered defect concentration of 1.4% and the full localization of the additional electrons at 8.3% defect concentration (see ESI for details[†]). The external isotropic pressure was considered as a further parameter that might determine the localization energy for single V_O and H_O defects in the $3 \times 3 \times 1$ supercell. Here our *ab initio* calculations predict the transition from localized mid-gap states to delocalized shallow donor-states with increasing external pressure for both defect types (Fig. 8(b)). The sensitivity of the localization energy to pressure is more pronounced in the case of the V_O defects. While the transition takes place at negative (expansive) pressure for the H_O defects, compressive pressures larger than 5 GPa are needed to enforce delocalization in the case of V_O defects. The origin of the pressure dependence of the

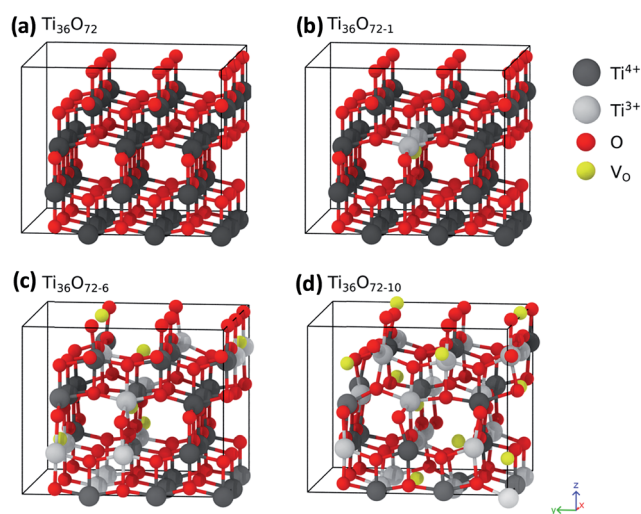


Fig. 7 (a–d) $3 \times 3 \times 1$ supercells of TiO_2 containing 0, 1, 6 and 10 V_O defects, respectively. The positions of the oxygen vacancies are indicated by yellow spheres, oxygen ions are shown in red and Ti ions in grey. Ti^{3+} centres are shown as bright grey spheres and Ti^{4+} ions as dark grey spheres.



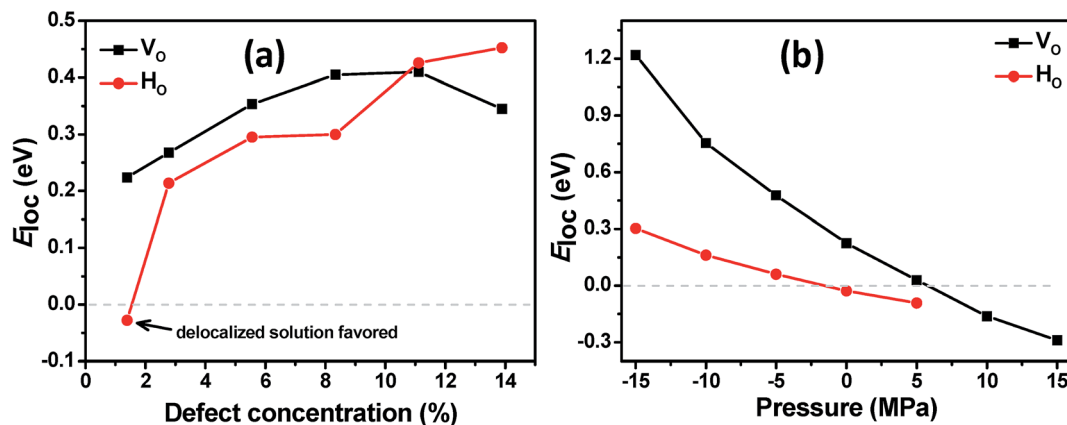


Fig. 8 Localization energy E_{loc} per defect for the excess charge carriers induced by V_O and H_O defects as a function of (a) defect concentrations and (b) external pressure for a single defect. Positive values of E_{loc} mean that the localized Ti^{3+} centers are more stable than the delocalized shallow donor states. For the H_O defects localized solutions could not be stabilized in the *ab initio* simulations at pressures >5 GPa.

localization energy can be traced back to the lattice distortion of the localized Ti^{3+} centers which is easier to be accommodated in an expanded lattice. Structural analysis shows that the lattice distortions are locally confined near the Ti^{3+} centers and can hence be considered as small polarons.²⁹

In the next step the electronic structure modification of TiO_2 depending on the concentration of V_O and H_O defects is investigated. The presence of localized Ti^{3+} centers can be associated with the formation of occupied mid gap states in the density of states (DoS). As shown in Fig. 9(a), at low concentrations of oxygen vacancies of about 1%, we find two mid gap states, 0.74 eV and 1.11 eV, below the conduction band minimum (CBM), which are formed by two localized Ti^{3+} centers in the vicinity of the respective oxygen vacancies. These are shown in Fig. 7 as grey spheres and their effect on the density of states is in good agreement with previous *ab initio* studies on single oxygen vacancies.³⁰ As discussed above, at the lowest considered concentration of H_O defects the delocalized solution is favored such that in this case no midgap state is

present in the DoS (Fig. 9(b)). At higher defect concentrations occupied midgap states are present for both defect types and the respective midgap state spectra broaden and shift down towards the valence band maximum, although the broadening of the spectrum is considerably more pronounced for the V_O defects. In order to facilitate the comparison, the DoS of the different defect concentrations in Fig. 9(a) and (b) were aligned with respect to the center of the O2s band which is only weakly affected by the presence of V_O and H_O defects, see ESI Fig. S2.†

We obtain qualitatively similar results employing the HSE06 hybrid functional as shown in Fig. S1 of the ESI.† Both methods predict the double peak in the midgap region for a single V_O defect and the considerably broadened and down shifted spectrum of defect states at higher V_O concentrations. In the case of the H_O defects, in both methods no midgap state is formed at low defect concentrations while at higher defect concentrations a relatively narrow spectrum of defect states forms below the CBM. Quantitatively, the main differences between the two approaches are the deviating predictions for

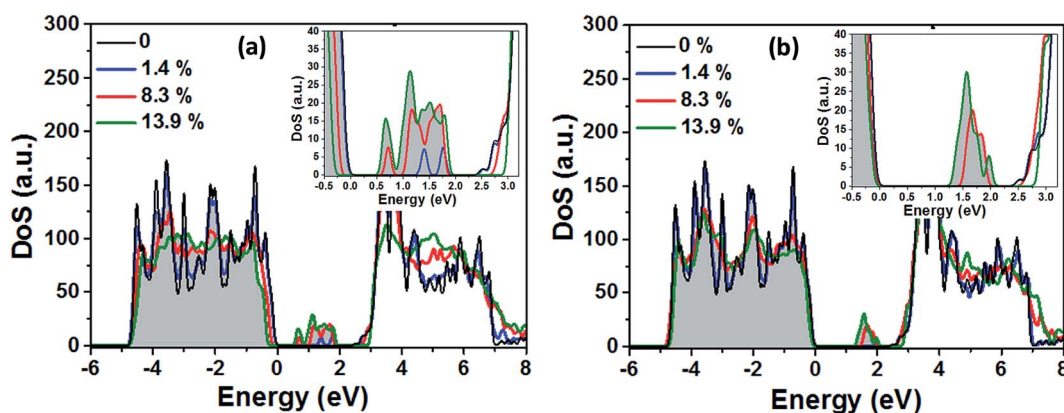


Fig. 9 Density of states (DoS) of anatase TiO_2 for different concentrations of oxygen vacancies V_O in (a) and substitutional H_O defects in (b). The band gap areas are enlarged and shown as insets. Shown are the densities of states for 0, 1, 6 and 10 defects in the $3 \times 3 \times 1$ supercell. This corresponds to defect concentrations of 0%, 1.4%, 8.3% and 13.9% with respect to the number of oxygen atoms. The highest occupied state of pristine TiO_2 sets the zero energy. Occupied energy levels are indicated by the grey shading.



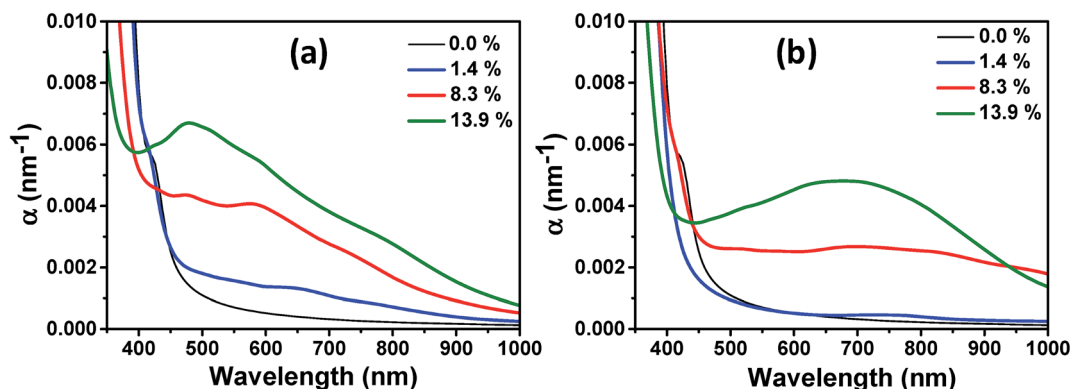


Fig. 10 Absorption coefficient α of anatase TiO_2 with different concentrations of (a) oxygen vacancies V_{O} and (b) substitutional H_{O} defects. A higher concentration of oxygen vacancies leads to a considerable photo-absorption in the visible spectrum. No saturation in the photo-absorption is observed up to the investigated vacancy concentrations. Note that the simulations indicate that already the defect free anatase TiO_2 seems to absorb visible light at the low wavelength limit. This inconsistency with the experiment is due to the underestimation of the electronic band gap by the employed PBE + U method which leads to a red-shift in the absorption spectrum.

the electronic band gap of pristine TiO_2 of 2.55 eV (PBE + U) and 3.77 eV (HSE06). Hence the PBE + U formalism underestimates, while the HSE06 functional overestimates the experimental value of ~ 3.4 eV.²²

Finally, we investigated the effect of V_{O} and H_{O} defects on the optical absorption below the absorption edge of pristine TiO_2 and the influence of the defect concentration. In Fig. 10(a), we show the wavelength dependent optical absorption coefficient for the V_{O} defects. Already at a low defect concentration of 1.4%, the absorption of photons with energies below the band gap energy of pristine TiO_2 is observed. With increasing defect concentration the absorption increases further and up to the investigated defect concentration of 13.9%, no saturation in the visible light absorption coefficient is seen, indicating that the degree of disorder is the crucial quantity that leads to the experimentally observed high photoabsorption. Consistent with the experimentally obtained DRS measurements a declining photoabsorption with increasing wavelength is observed. We note, however, that the simulated values are red-shifted with respect to the experimental data due to the underestimation of

the electronic band gap. The photoabsorption spectrum of different H_{O} defect concentrations is shown in Fig. 10(b). Here, no considerable photoabsorption in the band gap region of pristine TiO_2 is observed at a low defect concentration of 1.4% in accordance with the absence of a localized midgap state. At the higher defect concentrations photoabsorption in the visible light range sets in and again an increasing defect concentration leads to higher absorption coefficients. In contrast to the V_{O} defects and the experimental data the absorption coefficient decays much slower with increasing wavelength. This suggests that the hydrogen treated samples considered in this work mainly contain oxygen vacancies. This does not exclude their partial occupancy by substitutional hydrogen.

3.1 Photocatalytic and photoelectrochemical activity

The photocatalytic activity of all four samples was evaluated by measuring the time-dependent degradation of methylene blue (MB) under visible-light irradiation (Fig. 11(a)). From Fig. 11(b), we can see that the pristine TiO_2 sample shows poor photocatalytic activity in the visible-light. The degradation rate

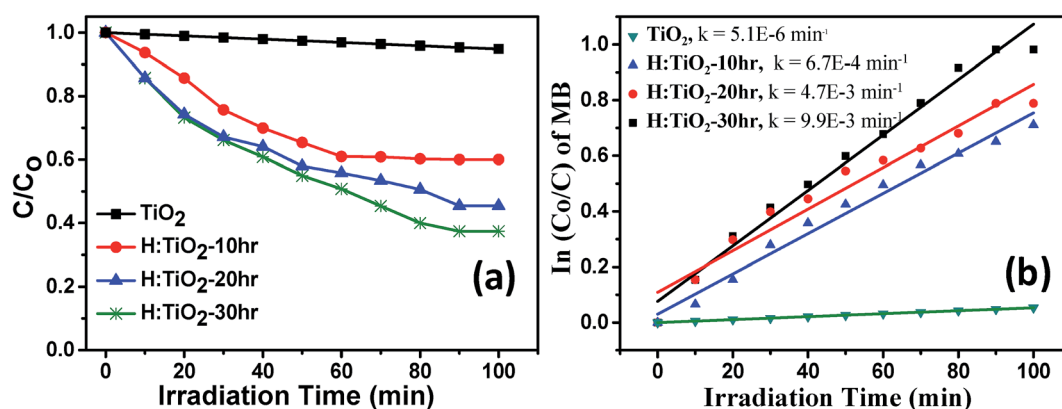


Fig. 11 (a) Solar-light driven photocatalytic decomposition of Methylene blue (b) rate constant calculation for pristine and hydrogen treated TiO_2 samples.



constant k of pristine TiO_2 was $\sim 5.1 \times 10^{-6} \text{ min}^{-1}$. This small value is attributed to the large band gap energy of TiO_2 . For the H: TiO_2 samples, the photodegradation activity increases with increasing the hydrogen treatment time as expected from the enhanced visible light absorption. The photodegradation rate constant k reaches the maximum $\sim 9.9 \times 10^{-3} \text{ min}^{-1}$ for the 30 h hydrogen treated sample. This value is approximately three orders of magnitude higher than that of pristine TiO_2 under visible-light irradiation. Further, we have also investigated the photocatalytic degradation efficiency of pure and hydrogen treated TiO_2 for colorless pollutants such as phenol. The phenol degradation efficiency with different photocatalysts as a function of visible light irradiation time is given in ESI Fig. S3.† To check the long stability of the defect generated in H: TiO_2 by hydrogen treatment when stored under ambient conditions, we used H: TiO_2 samples to re-examine the structural, optical and electrical properties and also used them for photocatalytic and photoelectrochemical application tests. We found that H: TiO_2 samples still exhibit the presence of Ti^{3+} and the enhanced photocatalytic activity for phenol degradation (Fig. S3 of the ESI†).

To determine the photoelectrochemical activity for solar hydrogen production through water splitting, thin films of pristine TiO_2 and H: TiO_2 powders were prepared using the spin coating technique on ITO substrates and converted into electrodes. The photoelectrochemical measurements were performed under visible light illumination ($\lambda = 380 \text{ nm}$) with an output intensity of 100 mW cm^{-2} through a tungsten lamp. The enhanced visible light photoactivity of H: TiO_2 was examined by measuring the linear sweep voltammetry scans under dark and illumination in the potential range of -0.5 to $+1.0 \text{ V vs. Ag/AgCl}$ with a scan rate of 20 mV s^{-1} . Fig. 12(a) shows the photocurrent density vs. applied potential (V vs. Ag/AgCl) curves for pristine and hydrogen treated TiO_2 samples collected in 1 M NaOH solution. In the case of pristine TiO_2 a very small photocurrent was obtained which is $\sim 35 \mu\text{A cm}^{-2}$ (at $1.0 \text{ V vs. Ag/AgCl}$). However, the H: TiO_2 samples show a large improvement in the photocurrent density ($\sim 0.56 \text{ mA cm}^{-2}$ at $1.0 \text{ V vs. Ag/AgCl}$) under the same experimental conditions.

To determine the intrinsic electrical properties of pristine TiO_2 and H: TiO_2 samples, thin films of TiO_2 were used as working electrodes for the Mott-Schottky ($1/C^2$ versus V_{app}) measurements. Mott-Schottky measurements were carried out at 1 kHz AC signal frequency in 1 M NaOH solution under dark conditions to calculate the donor density (N_D) and flat band potential (V_{FB}) by using the Mott-Schottky equation.⁴ Fig. 12(b) shows the Mott-Schottky plots for pristine and hydrogen treated TiO_2 samples. The positive slope of Mott-Schottky curves in all the samples indicated the n-type conductivity of the TiO_2 thin films. The donor density was estimated from the slopes of the Mott-Schottky curve using the equation,

$$N_D = \frac{2}{\epsilon\epsilon_0 q} \left[\frac{d(1/C^2)}{dV} \right]^{-1}$$

The calculated value of N_D , as estimated from the slopes of the Mott-Schottky curve, was found to increase with hydrogen incorporation. The hydrogen treated H: TiO_2 films exhibited significantly higher donor density, $5.5 \times 10^{17} \text{ cm}^{-3}$, compared to the pristine TiO_2 ($7.2 \times 10^{16} \text{ cm}^{-3}$) sample even though the phase structure of the material did not show any major changes. The enhanced donor density can be attributed to excess electrons provided by lattice defects such as oxygen vacancies (V_O) or oxygen vacancies that are occupied by atomic hydrogen (H_O). Our simulation shows that delocalized excess charge carriers are rather formed by the H_O defects at low defect concentrations. Since HR-TEM data show a highly defective surface of the H: TiO_2 samples, delocalized charge carriers can rather be expected in the bulk region of the nanocrystals, where the defect concentration should be considerably lower. The observed negative shift of flat band potential could be due to the substantially increased electron density, which is expected to shift the Fermi level of TiO_2 towards the conduction band.

Further, electrochemical impedance spectroscopic (EIS) measurements have been performed under visible light illumination to understand the effect of hydrogen treatment of TiO_2 on charge separation and recombination processes. EIS Nyquist plots of the pristine and H: TiO_2 samples are shown in Fig. 13. The EIS results show that only one semicircle was observed for each sample and thus can be fitted with the

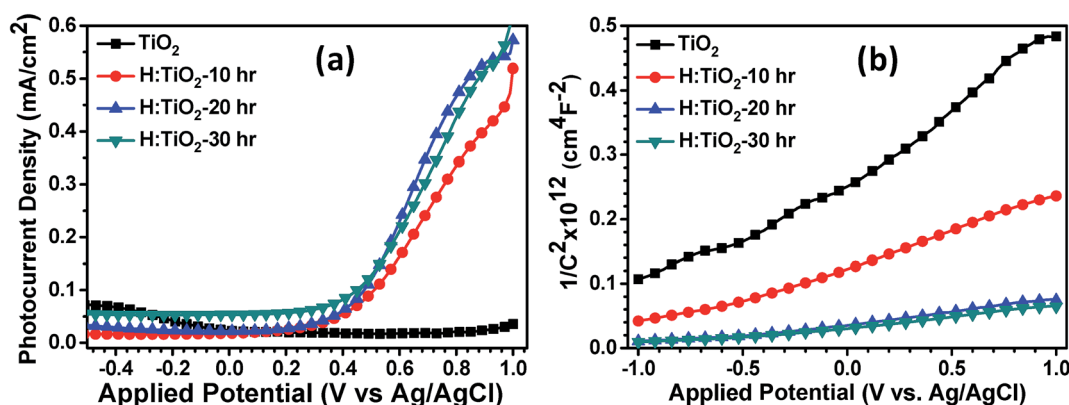


Fig. 12 (a) Photocurrent density vs. applied potential (V vs. Ag/AgCl) curves (b) Mott-Schottky plots for pristine and hydrogen treated TiO_2 samples collected in 1 M NaOH solution.



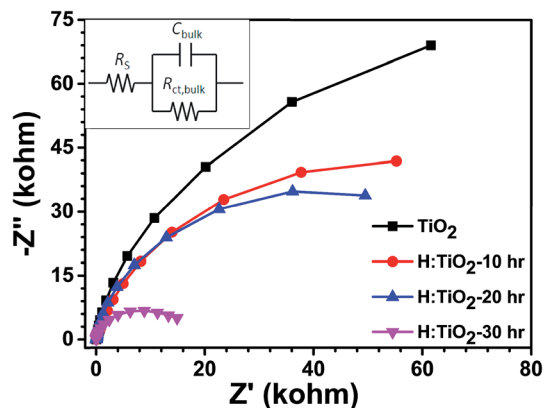


Fig. 13 EIS Nyquist plots of the pristine and hydrogen treated TiO_2 samples at an open bias condition under dark.

Randles equivalent circuit model (inset of Fig. 13)⁴⁹. In this model, the element R_s is the resistance related to charge transport and contains the resistance of the semiconductor catalyst, ITO substrate, the electrolyte and wire connections in the whole circuit. The elements of $R_{ct,bulk}$ and C_{bulk} are related to the charge transfer at the interface of the photoelectrode/electrolyte. A smaller radius of the semicircle represents a better charge transfer ability (*i.e.*, faster surface reaction kinetics).⁴⁹ As shown in Fig. 13, it is evident that the radii of semicircle on the real axis of Nyquist plots of H:TiO₂ treated in hydrogen for 30 h are much smaller than those for pristine and other TiO₂ samples, which indicates that the hydrogen treatment in TiO₂ reduces the semiconductor–electrolyte contact resistance and improves the charge transport. Therefore, the charge transport efficiency of H:TiO₂ samples increased significantly both on the surface (*i.e.*, surface reaction kinetics) and in the bulk, leading to an improved PEC activity. The smaller radii of the H:TiO₂ samples are presumably due to an increased electron density as obtained in the Mott–Schottky measurement which improves the electrical conductivity of the electrodes. The smaller arc radii in H:TiO₂ under illumination in EIS plots clearly indicate that the fast charge transfer occurs on the photoelectrodes.

Therefore, the significant improvement in the photocatalytic activity and photocurrent density after hydrogen treatment of TiO₂ nanocrystals shows that they can generate more electron–hole pairs in visible light and exhibit a stronger ability for electron–hole pair separation than pristine TiO₂. The observation of a small photocurrent in pristine TiO₂ using visible light illumination ($\lambda > 380$ nm) is due to the high band gap energy as the photons with energies less than the band gap energy ($E_g = 3.31$ eV) did not contribute to the excitation of valence band electrons to the conduction band to generate the electron–hole pairs. The DRS, EPR and Mott–Schottky measurements and DFT calculation clearly show that the reduction in the band gap of H:TiO₂ is likely due to the formation of midgap states induced by localized Ti³⁺ states. Therefore, the significant improvement in photocatalytic activity and photocurrent density can be explained by the surface disordering and defect formation after hydrogen treatment.

4. Conclusion

In summary, it has been shown that hydrogen treatment of TiO₂ under partial pressure conditions leads to an enhanced photocatalytic and photoelectrochemical response, which significantly depends on the duration of hydrogen treatment. DRS and EPR analyses of pristine and hydrogen treated TiO₂ nanocrystals show that the tailoring in properties of H:TiO₂ is due to surface oxygen-vacancies and Ti³⁺ states. Additionally, these modifications in properties induced a higher charge carrier concentration and a more negative flat band potential as compared to pristine TiO₂. The experimental studies were substantiated by *ab initio* calculations in order to gain a deeper understanding of the origin of enhanced visible light absorption due to Ti³⁺ centers and the conditions that favor the formation of localized or delocalized excess electrons due to oxygen vacancies. It was shown that with higher concentrations of V_O and H_O defects the spectrum of the induced midgap states broadens considerably and moves energetically downward towards the VBM. At the same time the visible light absorption increases and localization of the Ti³⁺ states becomes more favorable. Substitutional H_O defects at low concentrations were identified as candidates to provide delocalized charge carriers in TiO₂. This study provides a detailed overall picture covering experimental and theoretical aspects of the effect of hydrogen treatment on the structural, optical and electronic properties of the TiO₂ matrix and resulting improvements in the photoelectrochemical properties.

Author contributions

A. P. Singh and S. Basu conceived the idea, designed the experiments and worked out the overall structure of the manuscript. M. Mehta and N. Kodan prepared and characterized the samples and analyzed the data for the experimental part of the manuscript. S. Kumar performed the catalytic measurements and was involved in writing the particular section of the manuscript. A. Kaushal performed the HRTEM and analyzed the data. A. Dey and S. Krishnamurthy performed the XPS measurements and the XPS peak fitting and were involved in writing the particular section of the manuscript. L. Mayrhofer performed and analyzed the DFT calculations and was involved in writing the manuscript. M. Walter was involved in writing the revision of the manuscript and in discussing the DFT results. M. Moseler gave advice on the setup and analysis of the DFT calculations and was involved in the interpretation and discussion of the DFT results. The manuscript was written through contributions of all authors. All authors have given approval to the final version of the manuscript.

Acknowledgements

We gratefully acknowledge the financial support provided by the Department of Science and Technology, New Delhi India under the SERI and DST-UKERI programme and the New Indigo project InSOL. A. P. S. is grateful to the Department of Science & Technology, New Delhi, India for financial support in terms of INSPIRE Faculty award No. IFA12-PH-16. L. M. and M. M. kindly acknowledge the financial support under the FP7 project



“SOLAROGENIX” (NMP4-SL-2012-310333). The *ab initio* calculations were performed on the Joe cluster of Fraunhofer IWM and on JUROPA at the Julich Supercomputing Center (JSC). The authors gratefully acknowledge the computing time granted by the John von Neumann Institute for Computing (NIC) and provided on the supercomputer JUROPA at JSC.

References

- 1 A. Fujishima, T. N. Rao and D. A. Tryk, *J. Photochem. Photobiol., C*, 2000, **1**, 1–21.
- 2 A. P. Singh, S. Kumari, R. Shrivastav, S. Dass and V. R. Satsangi, *Int. J. Hydrogen Energy*, 2008, **33**, 5363–5368.
- 3 M. R. Hoffmann, S. T. Martin, W. Choi and D. W. Bahnemann, *Chem. Rev.*, 1995, **95**, 69–96.
- 4 R. Dholam, N. Patel, M. Adami and A. Miotello, *Int. J. Hydrogen Energy*, 2009, **34**, 5337–5346.
- 5 H. Zhu, J. Tao and X. Dong, *J. Phys. Chem. C*, 2010, **114**, 2873–2879.
- 6 R. Asahi, T. Morikawa, T. Ohwaki, K. Aoki and Y. Taga, *Science*, 2001, **293**, 269–271.
- 7 S. U. M. Khan, M. Al-Shahry and W. B. Ingler Jr, *Science*, 2002, **297**, 2243–2245.
- 8 V. Tiwari, J. Jiang, V. Sethi and P. Biswas, *Appl. Catal., A*, 2008, **345**, 241–246.
- 9 P. V. Kamat, M. Flumiani and A. Dawson, *Colloids Surf., A*, 2002, **202**, 269–279.
- 10 A. A. Nada, M. H. Barakat, H. A. Hamed, N. R. Mohamed and T. N. Veziroglu, *Int. J. Hydrogen Energy*, 2005, **30**, 687–691.
- 11 M. Takeuchi, H. Yamashita, M. Matsuoka, M. Anpo, T. Hirao, N. Itoh and N. Iwamoto, *Catal. Lett.*, 2000, **67**, 135–137.
- 12 F. Zuo, L. Wang, T. Wu, Z. Zhang, D. Borchardt and P. Feng, *J. Am. Chem. Soc.*, 2010, **132**, 11856–11857.
- 13 X. Chen, L. Liu, P. Y. Yu and S. S. Mao, *Science*, 2011, **331**, 746–750.
- 14 X. Chen, L. Liu, Z. Liu, M. A. Marcus, W. C. Wang, N. A. Oyler, M. E. Grass, B. Mao, P.-A. Glans, P. Y. Yu, J. Guo and S. S. Mao, *Sci. Rep.*, 2013, **3**, 1510.
- 15 H. Li, Z. Chen, C. K. Tsang, Z. Li, X. Ran, C. Lee, B. Nie, L. Zheng, T. Hung, J. Lu, B. Pan and Y. Y. Li, *J. Mater. Chem. A*, 2014, **2**, 229–236.
- 16 L. X. Zheng, H. Cheng, F. X. Liang, S. W. Shu, C. K. Tsang, H. Li, S. T. Lee and Y. Y. Li, *J. Phys. Chem. C*, 2012, **116**, 5509–5515.
- 17 Z. Wang, C. Yang, T. Lin, H. Yin, P. Chen, D. Wan, F. Xu, F. Huang, J. Lin, X. Xie and M. Jiang, *Adv. Funct. Mater.*, 2013, **23**, 5444–5450.
- 18 A. Mettenborger, T. Singh, A. P. Singh, T. T. Jarvi, M. Moseler, M. Valldor and S. Mathur, *Int. J. Hydrogen Energy*, 2014, **39**, 4828–4835.
- 19 H. Wu, C. Xu, J. Xu, L. Lu, Z. Fan, X. Chen, Y. Song and D. Li, *Nanotechnology*, 2013, **24**, 455401.
- 20 A. Sasinsk, T. Singh, S. Wang, S. Mathur and R. Kraehnert, *J. Vac. Sci. Technol., A*, 2015, **33**, 01A152.
- 21 A. Fujishima, X. T. Zhang and D. A. Tryk, *Surf. Sci. Rep.*, 2008, **63**, 515–582.
- 22 C. D. Valentin, G. Pacchioni and A. Selloni, *J. Phys. Chem. C*, 2009, **113**, 20543–20552.
- 23 A. P. Singh, S. Kumari, Sonal, R. Shrivastav, S. Dass and V. R. Satsang, *J. Sci. Conf. Proc.*, 2009, **1**, 82–85.
- 24 G. Kresse and J. Furthmüller, *Phys. Rev. B: Condens. Matter Mater. Phys.*, 1996, **54**, 11169–11186.
- 25 G. Kresse and D. Joubert, *Phys. Rev. B: Condens. Matter Mater. Phys.*, 1999, **59**, 1758–1775.
- 26 P. E. Blöchl, *Phys. Rev. B: Condens. Matter Mater. Phys.*, 1994, **50**, 17953–17979.
- 27 S. L. Dudarev, G. A. Botton, S. Y. Savrasov, C. J. Humphreys and A. P. Sutton, *Phys. Rev. B: Condens. Matter Mater. Phys.*, 1998, **57**, 1505–1509.
- 28 B. J. Morgan and G. W. Watson, *Surf. Sci.*, 2007, **601**, 5034–5041.
- 29 B. J. Morgan, D. O. Scanlon and G. W. Watson, *J. Mater. Chem.*, 2009, **19**, 5175–5178.
- 30 E. Finazzi, C. D. Valentin, G. Pacchioni and A. Selloni, *J. Chem. Phys.*, 2008, **129**, 154113.
- 31 M. Setvin, C. Franchini, X. Hao, M. Schmid, A. Janotti, M. Kaltak, C. G. Van de Walle, G. Kresse and U. Diebold, *Phys. Rev. Lett.*, 2014, **113**, 086402.
- 32 M. Fox, *Optical Properties of Solids*, Oxford University Press, 2001.
- 33 M. Gajdoš, K. Hummer, G. Kresse, J. Furthmüller and F. Bechstedt, *Phys. Rev. B: Condens. Matter Mater. Phys.*, 2006, **73**, 045112.
- 34 K. M. Mackay, *Hydrogen Compounds of the Metallic Elements*, E and F N Spon, London, UK, 1966, p. 71.
- 35 P. Raghunath, W. F. Huang and M. C. Lin, *J. Chem. Phys.*, 2013, **138**, 154705.
- 36 M. Ocana, J. V. Garcia-Ramos and C. J. Serna, *J. Am. Ceram. Soc.*, 1992, **75**, 2010–2016.
- 37 M. Crocker, R. H. M. Herold, A. E. Wilson, M. Mackay, C. A. Emeis and A. M. Hoogendoorn, *J. Chem. Soc., Faraday Trans.*, 1996, **92**, 2791–2798.
- 38 P. Jonsen, *Colloids Surf.*, 1989, **36**, 127–132.
- 39 H. H. Nahm and C. H. Park, *J. Korean Phys. Soc.*, 2010, **56**, 485–489.
- 40 F. Filippone, G. Mattioli, P. Alippi and A. Amore Bonapasta, *Phys. Rev. B: Condens. Matter Mater. Phys.*, 2009, **80**, 245203.
- 41 U. Aschauer and A. Selloni, *Phys. Chem. Chem. Phys.*, 2012, **14**, 16595.
- 42 S. M. Prokes, J. L. Gole, X. Chen, C. Burda and W. E. Carlos, *Adv. Funct. Mater.*, 2005, **15**, 161–167.
- 43 J. Strunk, W. C. Vining and A. T. Bell, *J. Phys. Chem. C*, 2010, **114**, 16937–16945.
- 44 I. Luciu, R. Bartali and N. Laidani, *J. Phys. D: Appl. Phys.*, 2012, **45**, 345302.
- 45 U. Diebold, *Surf. Sci. Rep.*, 2003, **48**, 53–229.
- 46 G. Wang, H. Wang, Y. Ling, Y. Tang, X. Yang, R. C. Fitzmorris, C. Wang, J. Z. Zhang and Y. Lim, *Nano Lett.*, 2011, **11**, 3026–3033.
- 47 X. Liu, H. Xu, L. R. Grabstanowicz, S. Gao, Z. Lou, W. Wang, B. Huang, Y. Dai and T. Xu, *Catal. Today*, 2014, **225**, 80–89.
- 48 A. Naldoni, M. Allieta, S. Santangelo, M. Marelli and F. Fabbri, *J. Am. Chem. Soc.*, 2012, **134**, 7600–7603.
- 49 B. Klahr, S. Gimenez, F. Fabregat-Santiago, T. Hamann and J. Bisquert, *J. Am. Chem. Soc.*, 2012, **134**, 4294.

